Biosensors and Bioelectronics 192 (2021) 113505

Contents lists available at ScienceDirect

Biosensors and Bioelectronics

journal homepage: www.elsevier.com/locate/bios

Dual-signal electrochemiluminescence immunosensor for Neuron-specific enolase detection based on "dual-potential" emitter $Ru(bpy)_3^{2+}$ functionalized zinc-based metal-organic frameworks

Xue Dong [a], Yu Du [b], Guanhui Zhao [a], Wei Cao [b], Dawei Fan [b], Xuan Kuang [b], Qin Wei [b,*], Huangxian Ju [b,c,**]

[a] Key Laboratory of Interfacial Reaction & Sensing Analysis in Universities of Shandong, School of Chemistry and Chemical Engineering, University of Jinan, Jinan, 250022, Shandong, China
[b] Collaborative Innovation Center for Green Chemical Manufacturing and Accurate Detection, University of Jinan, Jinan, 250022, Shandong, China
[c] State Key Laboratory of Analytical Chemistry for Life Science, School of Chemistry and Chemical Engineering, Nanjing University, Nanjing, 210023, China

ARTICLE INFO

Keywords:
Dual-potential
Ratiometric
Metal-organic framework
Electrochemiluminescence
Neuron-specific enolase

ABSTRACT

Neuron-specific enolase (NSE) is the preferred marker for monitoring small cell lung cancer and neuroblastoma. We devised a dual-signal ratiometric electrochemiluminescence (ECL) sensing strategy for sensitive detection of NSE. In this work, Ru $(bpy)_3^{2+}$ functionalized zinc-based metal-organic framework (Ru-MOF-5) nanoflowers (NFs) with *plentiful* carboxyl groups provide an excellent biocompatible sensing platform for the construction of immunosensor. Importantly, Ru-MOF-5 NFs possess stable and efficient "dual-potential" ECL emission of cathode (−1.5 V) and anode (1.5 V) in the existence of co-reactant $K_2S_2O_8$. Simultaneously, the cathode ECL emitter ZnO-AgNPs are employed as the secondary antibody marker, whose participation amplify the cathode ECL signal as well attenuate the anode ECL emission of Ru-MOF-5 NFs. By monitoring the ECL dual-signal of −1.5 V and 1.5 V and calculating their ratios, a ratiometric strategy of quantified readout proportional is implemented for the proposed immunosensor to precise analyze NSE. Based on optimization conditions, the ECL immunosensor displays the wide linear range of 0.0001 ng/mL to 200 ng/mL and the minimum detection limit is 0.041 pg/mL. The "dual-potential" ratiometric ECL immunosensor effectively reduces system error or background signal by self-calibration from both emissions and improves detection reliability. The dual-signal ratiometric strategy with satisfactory reproducibility and stability provides further development possibilities for other biomolecular detection and analysis.

1. Introduction

Neuron-specific enolase (NSE) present in neural and neuroendocrine tissues is one of the enolases involved in the glycolysis pathway (Isgrò et al., 2015). Normal human serum has a NSE content of 5–15 ng/ml, while that of patients with small cell lung cancer (SCLC) is significantly increased (Bandyopadhyay et al., 2014; Leff et al., 2015). The clinical study showed that when the initial level of NSE is lower than 100 ng/ml, the prognosis is favorable and the survival rate is high. Conversely, if the initial level of NSE is higher than the above values, the prognosis is poor and the survival rate is observably lower. Therefore, it is necessary to propose a sensitive and wide linear detection strategy for the detection of NSE in serum.

Electrochemiluminescence (ECL) immunosensor has superiorities of simple operation, excellent sensitivity and specificity (Li et al., 2017; Liu et al., 2015; Lv et al., 2019). However, the ECL sensing strategy of single-probe or single-signal may inevitably lead to positive or negative deviations in the process of trace analyses due to external change, which reduces the reliability of detection. The advent of "dual-potential" or "dual-wavelength" ratiometric ECL sensors effectively reduce or even eliminate external interference and improve detection reliability, especially for low concentrations or targets in complex biological systems.

* Corresponding author.
** Corresponding author. Collaborative Innovation Center for Green Chemical Manufacturing and Accurate Detection, University of Jinan, Jinan, 250022, Shandong, China.
E-mail addresses: sdjndxwq@163.com (Q. Wei), hxju@nju.edu.cn (H. Ju).

https://doi.org/10.1016/j.bios.2021.113505
Received 22 June 2021; Accepted 12 July 2021
Available online 16 July 2021

However, since the result of the ECL sensor is only the change of ECL strength, external environmental or system factors may affect the ECL signal output. The advent of "dual-potential" or "dual-wavelength" ratiometric ECL strategies effectively reduce or even eliminate external interference by self-calibration from both emissions (Feng et al., 2017b; Fu et al., 2017; Shang et al., 2020; Ye et al., 2018). ECL ratiometric immunosensor provides more accurate analysis to normalize variation in environmental changes. In addition, the ECL sensing strategy of single-probe or single-signal may inevitably lead to positive or negative deviations in the process of trace analyses due to external change (Li et al., 2019, 2020; Zhou et al., 2021). False positive or negative errors will affect the reliability of target detection, and it is difficult to be detected in single-signal mode. When the cathode and anode signals are detected at the same time and the ratio is calculated, the output of three results will confirm each other. If there is any error, it will be found and corrected in time. This means that the ratiometric ECL sensor can effectively reduce the false positive or negative errors probability of single signal mode. The ratiometric strategy can acquire more credible outcomes in intricate environments than conventional ECL immunosensor. Under normal circumstances, the "dual-potential" ratiometric ECL immunosensor based on a pair of independent luminophores emit two ECL signal peaks at two potentials that differ greatly, such as the cathode and the anode. But in recent years, there are few reports of "dual-potential" ECL emission from single luminophore, which is of great significance for further promoting the development of ECL immunosensor.

In recent years, a growing number of metal-organic frameworks (MOFs) have been synthesized and researched (Forgan et al., 2012; Wang et al., 2020). The important reason that it can be paid attention to and explored by researchers is its abundant functional group and easy to be functionalized (Farzad et al., 2020). Ru $(bpy)_3^{2+}$ functionalized Zn-based MOF (Ru-MOF-5) nanoflowers (NFs) with the large specific surface and abundant functional groups are easy to synthesize. In particular, it has a large number of carboxyl groups, which improves the binding rate and loading rate with biomolecules, such as antibodies and antigens. More importantly, Ru-MOF-5 NFs are discovered with strong ECL emission from the anode (1.5 V) in pure PBS buffer. Whereafter, the distinct "dual-potential" ECL emission of cathode (−1.5 V) and anode (1.5 V) is detected in the presence of $K_2S_2O_8$ in PBS buffer. The MOF material Ru-MOF-5 NFs with "dual-potential" ECL emission provides the foundation for the fabrication of dual-signal ECL immunosensors.

An ECL quencher is any species that causes the luminophore to stop luminescing. There are several ways this can happen, but there are two broad categories: chemical reactions and energy transfer (Adsetts et al., 2020; Gao et al., 2019; Guo et al., 2020). However, which method is operating is going to depend on the luminophore and the quencher. The new ECL reagent ZnO-AgNPs acts as both cathodic luminophore and ECL quencher. The quenching is caused by ECL resonance energy transfer (ECL-RET) between Ru-MOF-5 NFs (donor) and ZnO-AgNPs (acceptor). Ru-MOF-5 NFs generate an ECL emission peak at 624 nm, simultaneously, ZnO-AgNPs produce ultraviolet visible (UV–Vis) absorption at 377 nm–800 nm. The ECL emission spectra of Ru-MOF-5 NFs and the UV–Vis absorption spectra of ZnO-AgNPs partially overlap, which is the reason for the occurrence of ECL-RET.

Hence, a ratiometric ECL immunosensor was fabricated for accurate quantitative analysis of NSE based on "dual-potential" luminophore. Ru-MOF-5 NFs as the substrate releases "dual-potential" signals of cathode and anode. While the anode and cathode signals of immunosensor are respectively reduced and enhanced due to the effect of the cathodic luminophore ZnO-AgNPs that was employed as the secondary antibody (Ab_2) marker. The ratiometric ECL immunosensor was constructed using the ratio of the cathode and anode ECL signals. The ratiometric immunosensor displayed great sensitivity and favorable anti-interference performance.

2. Experimental section

2.1. Preparation of Ru-MOF-5 NFs

MOF-5 NFs were prepared based on reference and the synthesis steps were as follows (Zhao et al., 2014): $Zn(NO_3)_2{\cdot}6H_2O$ (2 mmol) and PTA (1 mmol) were dissolved in the solvent DMF (the molar ratio of DMF to PTA is 258.5:1). Afterwards, TEA was tardily dropped in the above mixture (the molar ratio of TEA to PTA is 7.91:1) and mixed for 2 h under ambient temperature. The obtained white product was separated at 8000 r/min for 5 min and washed 3 times with DMF and ultrapure water to remove unreacted inorganic salts and organic acids. Finally, MOF-5 NFs were placed in a vacuum oven to dry at 50 °C and kept at 4 °C for subsequent use.

Ru-MOF-5 NFs were synthesized on the basis of MOF-5 NFs and the synthesis steps were as follows: 200 mg of MOF-5 NFs and 2 mL of Ru $(bpy)_3^{2+}$ (50 mmol/L) were added into 30 mL of DMF. The obtained solution was stirred for 8 h at 70 °C in the oil bath. Subsequently, the obtained orange-yellow solution was centrifuged at 8000 r/min for 8 min and washed 3 times with DMF and ethanol. In the end, Ru-MOF-5 NFs were placed in a vacuum oven to dry at 50 °C and kept at 4 °C in order to subsequent usage.

2.2. Preparation of ZnO-AgNPs

ZnO-AgNPs were prepared based on reference and the synthesis steps were as follows (Ghosh et al., 2012; Zhang et al., 2010): 0.9855 g of Zn $(CH_3COO)_2{\cdot}2H_2O$ was added into 45 ml of diethylene glycol (DEG) and then acutely stirred for 30 min under ambient temperature. The above mixture was stirred for 1 h at 180 °C until an ivory solution occurred, that indicated the formation of ZnO. The obtained product was centrifuged at 6000 r/min for 1.5 h and washed 3 times with ethanol. In fine, ZnO was placed in a vacuum oven to dry and kept at 4 °C for subsequent usage.

25 mg of ZnO was dissolved in 10 ml of chitosan solution (involving 10 ml of ultrapure water and 10 mg of chitosan) and stirred for 1 h. Then the solution was separated and rinsed to get rid of unbound chitosan. Subsequently, the precipitate was dispersed in 10 ml of a mixture containing $AgNO_3$ (4 mmol/L) and sodium citrate (1 mmol/L) and mixed for 1 h. The product was separated and rinsed to get rid of unbound $AgNO_3$. The above steps were repeated in order to bind enough $AgNO_3$ on ZnO. Subsequently, the sodium borohydride solution was slowly added under stirring until the yellow solution appeared. Next, the obtained ZnO-AgNPs were separated and rinsed with ethanol. Lastly, the products were placed in a vacuum oven to dry and kept at 4 °C in order to subsequent usage.

2.3. Preparation of Ab_2-ZnO-AgNPs

2 mg of ZnO-AgNPs was dissolved into 0.5 mL of PBS buffer including 20 mmol of 1-ethyl-3-(3-dimethylaminopropyl) carbodiimide (EDC) and 10 mmol of N-hydroxysuccinimide (NHS) and then shaken at 4 °C for 2 h. Next, 0.5 mL of 1 mg/mL Ab_2 was dispersed in the above mixture as well as shaken for 24 h at 4 °C. Afterwards, adding 0.15 mL of BSA (1%) blocked non-specific binding sites on ZnO-AgNPs. At length Ab_2-ZnO-AgNPs were centrifuged and washed once then placed in 0.5 mL of PBS (pH 7.5) and stored at 4 °C in order to subsequent usage.

2.4. Preparation of the ECL immunosensor

The fabrication of ECL immunosensors was shown in Scheme 1. Firstly, 8 μL of the dispersed Ru-MOF-5 NFs was dispersed on the polished electrode surface and placed for half an hour. Subsequently, 4 μL of activator EDC/NHS solution (EDC = 400 mmol/L, NHS = 100 mmol/L) was added to the electrode to activate the carboxyl group on the surface of Ru-MOF-5 NFs. Then 8 μL of primary antibody (Ab_1) was

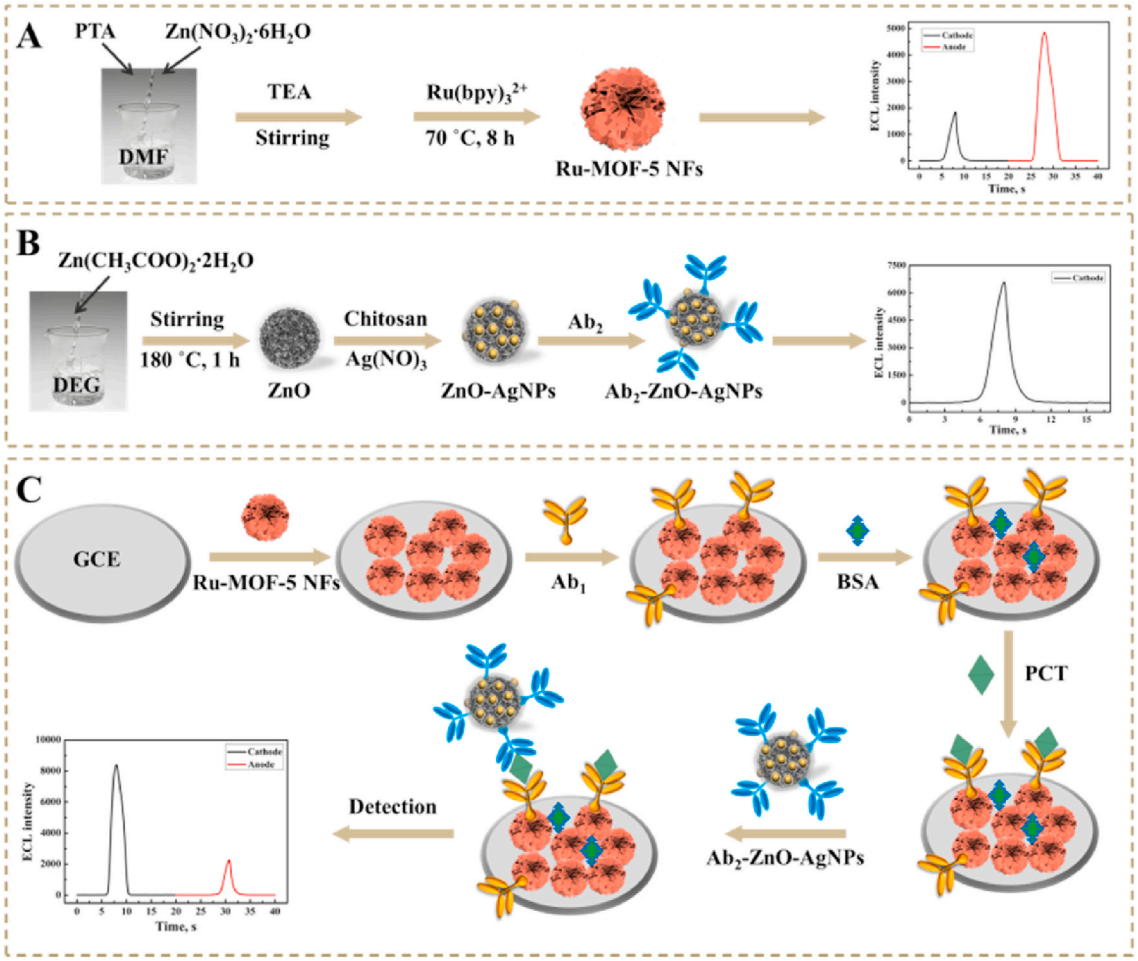

Scheme 1. The preparation of Ru-MOF-5 NFs (A) and Ab_2-ZnO-AgNPs (B); The schematic diagram of ECL immunosensor fabrication (C).

immobilized on GCE surface through binding to the carboxyl on the Ru-MOF-5 NFs and placed in refrigerator of 4 °C for 1 h. Next, 3 μL of BSA (1%) was dispersed on modified electrode for blocking nonspecific binding sites on the substrate material and dried at 4 °C. The electrode was rinsed with the PBS buffer (pH 7.5) to get rid of excess BSA. The next step was to incubate 8 μL NSE of varying concentrations on the GCE at 4 °C for 2 h in order to ensure sufficient binding to the antibody. Finally, 8 μL of Ab_2-ZnO-AgNPs was added into the GCE and placed at 4 °C for 2 h. Similarly, the GCE surface ought to be cautiously rinsed with PBS buffer (pH 7.5) to get rid of unbound Ab_2-ZnO-AgNPs. The fabricated "dual-potential" ECL immunosensors were kept at 4 °C in order to subsequent usage.

3. Results and discussions

3.1. Characterization of Ru-MOF-5 NFs

As shown in Fig. 1A, the complex size and morphology were measured and confirmed with SEM. The nano-flower-shaped MOF-5 is composed of irregularly interspersed flakes, and the thickness of the flakes is about 20–50 nm. Compared to MOF-5, the addition of Ru has made the MOF-5 curved and dense (Fig. 1B). The structures of the obtained MOF-5 and Ru-MOF-5 crystals are confirmed with XRD (Fig. 1C). The XRD spectrum can infer that the addition of Ru does not cause excessive changes in the crystalline structure of MOF-5. The Fourier transform infrared spectroscopy (FT-IR spectrum) is used to record IR absorption spectra of MOF-5 and Ru-MOF-5 (Fig. 1D). The two characteristic strong peaks located at 1585, 1570 and 1390, 1402 cm^{-1} correspond to the asymmetric and symmetric extension vibration peaks of $–COO^-$, respectively. The 1505 cm^{-1} can be associated with the extension vibration of C═C. The 821, 827 and 741, 729 cm^{-1} can be put down to out-of-plane deformation vibrations of C–H as well as the band of 741 and 729 cm^{-1} is obviously stronger than 821 and 827 cm^{-1} (SavićBiserčić et al., 2019). In addition, the elements composition of Ru-MOF-5 is farther confirmed through energy dispersive X-ray (EDX) characterization and element mapping. As shown in Fig. S1, the elements of C, O, Zn, and Ru are evenly distributed, and the percentage of various elements is also presented in Fig. S2.

XPS measurement was used to further research the chemical property and constitution of Ru-MOF-5 NFs. The survey spectrum of Ru-MOF-5 NFs and the spectrums of Zn, C, O and Ru are shown in Fig. S3. The peaks located at 1022.35 and 1045.35 eV correspond to Zn $2p_{3/2}$ and Zn $2p_{1/2}$. Two peaks located at 283.75 and 288.45 eV in the C 1s XPS spectra are attributed to the hydrocarbon and the carboxylate (–COO), respectively. And the O 1s peak centered at 532.65 eV is also associated with –COO. There are two peaks associated with Ru $3d_{5/2}$ and Ru $3d_{3/2}$ located at 281.15 and 284.65 eV, respectively. And the peak centered at 476.15 eV corresponds to Ru 3p.

3.2. Characterization of ZnO-AgNPs

The morphology, crystal structure and element distribution of ZnO and ZnO-AgNPs were observed by means of SEM, XRD and mapping. The SEM image reveals that spherical ZnO particles are uniformly dispersed between 75 and 125 nm, and the average size is 100 nm (Fig. 2A). AgNPs were characterized by Transmission Electron

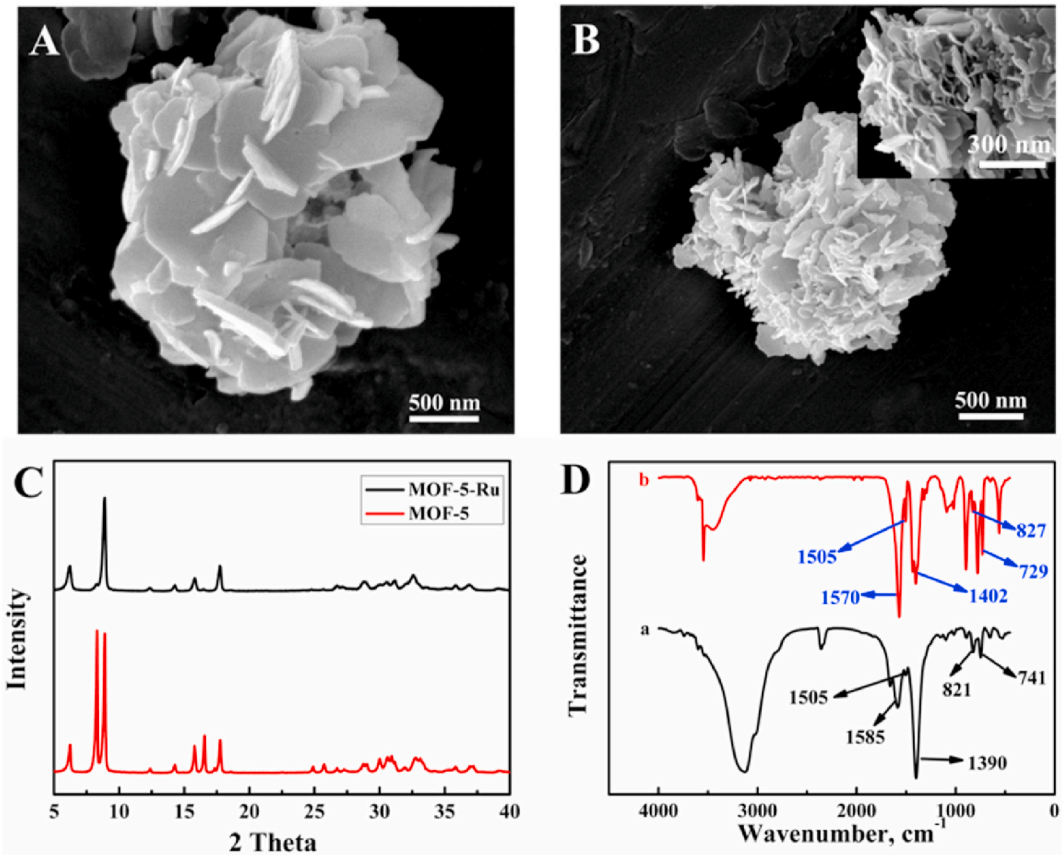

Fig. 1. SEM image of MOF-5 NFs (A) and Ru-MOF-5 NFs (B); XRD patterns of MOF-5 and Ru-MOF-5 NFs (C); FT-IR spectrum of MOF-5 (a) and Ru-MOF-5 NFs (b) (D).

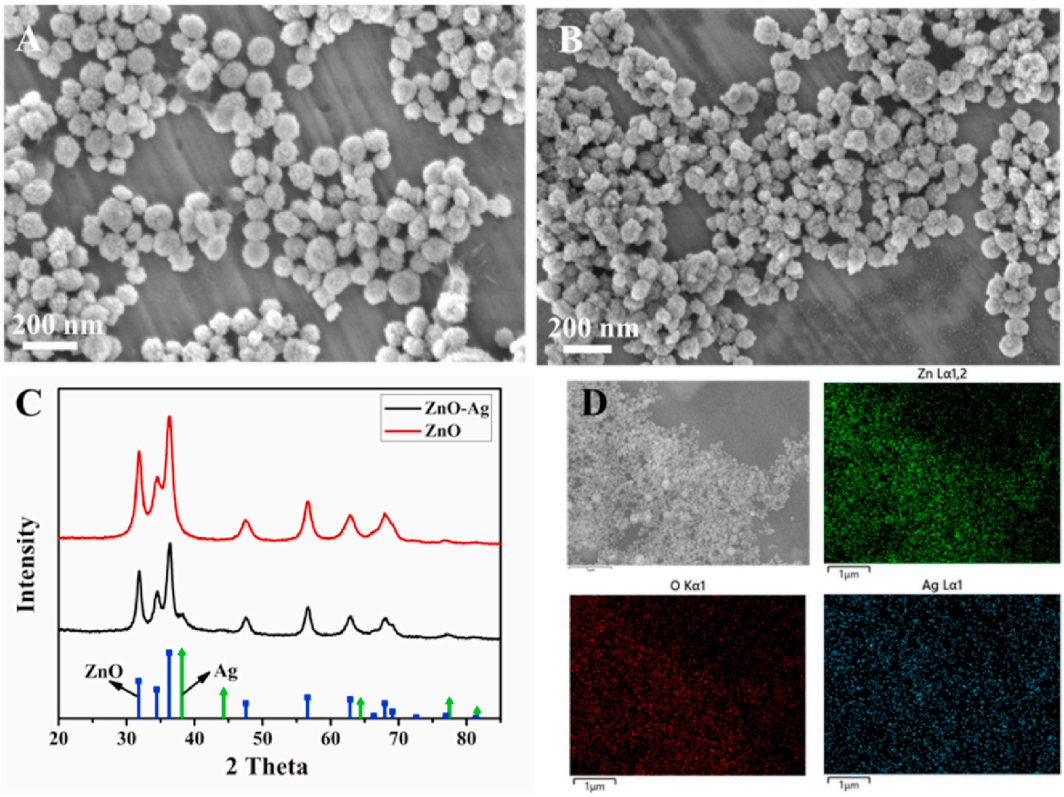

Fig. 2. SEM images of ZnO (A) and ZnO-AgNPs (B); XRD patterns of ZnO and ZnO-AgNPs (C); Mapping images of Zn, O, Ag of ZnO-AgNPs (D).

Microscope (TEM). As shown in Fig. S4, it can be seen that AgNPs are granular with a diameter of about 20 nm. The image of ZnO-AgNPs clearly proves that AgNPs are loaded on ZnO (Fig. 2B). The XRD pattern in Fig. 2C confirms the structure of ZnO and ZnO-AgNPs crystals. The distinct peaks at 2θ = 31.83°, 34.51°, 36.31°, 47.44°, 56.64°, 62.85° and 67.95° correspond to (100), (022), (101), (102), (110), (103) and (112) respectively, which correspond to Bragg reflections of the standard wurtzite structure of ZnO (JCPDS card 36–1451) (Ghosh et al., 2012). The peaks at 2θ = 37.5°, 44.3° correspond to (111), (200) of AgNPs, which prove the successful formation of ZnO and ZnO-AgNPs. Simultaneously, the elements composition of the synthesized material is farther determined through EDX characterization and element mapping. The elements of Zn, O and Ag are evenly distributed in Fig. 2D. The percentage of various elements is also presented in Fig. S5.

XPS measurement was executed to research the chemical property and constitution of ZnO-AgNPs nanocomposite (Huang et al., 2020; Raja et al., 2020). The XPS spectrums of elements Zn, O, Ag, C and N are exhibited in Fig. 3A–E, respectively. The peaks located at 1021.84 and 1044.94 eV correspond to Zn $2p_{3/2}$ and Zn $2p_{1/2}$ confirming the presence of Zn^{2+} on the samples surface (Fig. 3A). Two peaks located at 529.85 and 530.10 eV in the O 1s XPS spectra are attributed to lattice oxygen of ZnO and oxygen of surface hydroxyl groups, respectively (Fig. 3B). There are two peaks associated with Ag^0 $3d_{5/2}$ and Ag^0 $3d_{3/2}$ located at 367.51 and 373.51 eV, respectively, which proves that AgNPs in ZnO-AgNPs exist in the form of Ag^0 (Fig. 3C). The XPS spectrum of C exhibits three peaks located at 285.01, 286.41 and 289.21 eV (Fig. 3D), respectively. The peak centered at 285.01 eV corresponds to C–C and C–H linkages, 286.41 eV is attributed to C–OH linkage, and the peak at 289.21 eV is derived from C═O and [–O–C–O–] in chitosan polymer. The N 1s peak centered at 399.41 eV (Fig. 3E) may be associated with $–NH_2$ and N–C═O of chitosan.

3.3. Mechanism investigation of the immunoassay

The luminescence mechanism of Ru-MOF-5 NFs and ZnO-AgNPs double luminophores in this work was explored. The double potential luminescence of Ru-MOF-5 NFs is essentially the reaction of Ru $(bpy)_3^{2+}$ that reacted with TEA and $K_2S_2O_8$ to generate anode and cathode ECL signals. Instead of in the PBS buffer, TEA was inside Ru-MOF-5 NFs where the reaction path between Ru $(bpy)_3^{2+}$ and TEA was greatly shortened. Different from the reaction on electrode surface, the reaction efficiency between TEA and Ru $(bpy)_3^{2+}$ was notably enhanced. There was a majority of Ru $(bpy)_3^{2+}$ that reacts directly and rapidly with TEA thereby producing a higher ECL intensity. But there was still a minority of Ru $(bpy)_3^{2+}$ reacting with $K_2S_2O_8$ in PBS buffer to emit cathode ECL signal. Based on the literature and our experimental results, a possible mechanism of anode and cathode ECL luminescence systems based on Ru $(bpy)_3^{2+}$ were described as follows. Route 1 and Route 2 show the anodic and cathodic ECL excitation of Ru $(bpy)_3^{3+}$, respectively. Among them, route 2 shows two kinds of cathodic ECL emission mechanisms including oxidation followed reduction (eqs (2b) and (2c)) and reduction followed oxidation (eqs (2d) and (2e)). In the two routes, TEA and $S_2O_8^{2-}$ were used as co-reactants to severally react with Ru $(bpy)_3^{3+}$ to generate Ru $(bpy)_3^{2+}$* (Shi et al., 2017; Zhao et al., 2019).

Route 1:

$$Ru(bpy)_3^{2+} - e^- \rightarrow Ru(bpy)_3^{3+} \quad (1a)$$

$$TEA - e^- \rightarrow TEA^+ \quad (1b)$$

$$TEA^+ \rightarrow TEA^* + H^+ \quad (1c)$$

$$Ru(bpy)_3^{3+} + TEA^* \rightarrow [Ru(bpy)_3^{2+}]^* \quad (1d)$$

$$[Ru(bpy)_3^{2+}]^* \rightarrow Ru(bpy)_3^{2+} + h\nu \quad (1e)$$

Route 2:

$$S_2O_8^{2-} + e^- \rightarrow SO_4^{2-} + SO_4^{\bullet-} \quad (2a)$$

$$Ru(bpy)_3^{2+} + SO_4^{\bullet-} \rightarrow Ru(bpy)_3^{3+} + SO_4^{2-} \quad (2d)$$

$$Ru(bpy)_3^{3+} + e^- \rightarrow [Ru(bpy)_3^{2+}]^* \quad (2e)$$

$$Ru(bpy)_3^{2+} + e^- \rightarrow Ru(bpy)_3^{+} \quad (2b)$$

$$Ru(bpy)_3^{+} + SO_4^{\bullet-} \rightarrow [Ru(bpy)_3^{2+}]^* + SO_4^{2-} \quad (2c)$$

$$[Ru(bpy)_3^{2+}]^* \rightarrow Ru(bpy)_3^{2+} + h\nu \quad (2f)$$

ZnO-AgNPs labeled on the secondary antibody mainly played the roles of emitting the cathode ECL signal and quenching the ECL signal of Ru-MOF-5 NFs. The luminescence mechanism of ZnO-AgNPs nanocomposite as a novel ECL luminophore has been investigated (Route 3). $S_2O_8^{2-}$ and ZnO-AgNPs were reduced to $SO_4^{\bullet-}$ and ZnO-AgNPs$^{\bullet-}$, respectively, whose reduction products interact to form excited state ZnO-AgNPs*. ZnO-AgNPs* released energy back to the ground state and generated ECL emission (Feng et al., 2017a; Wang et al., 2012).

Route 3:

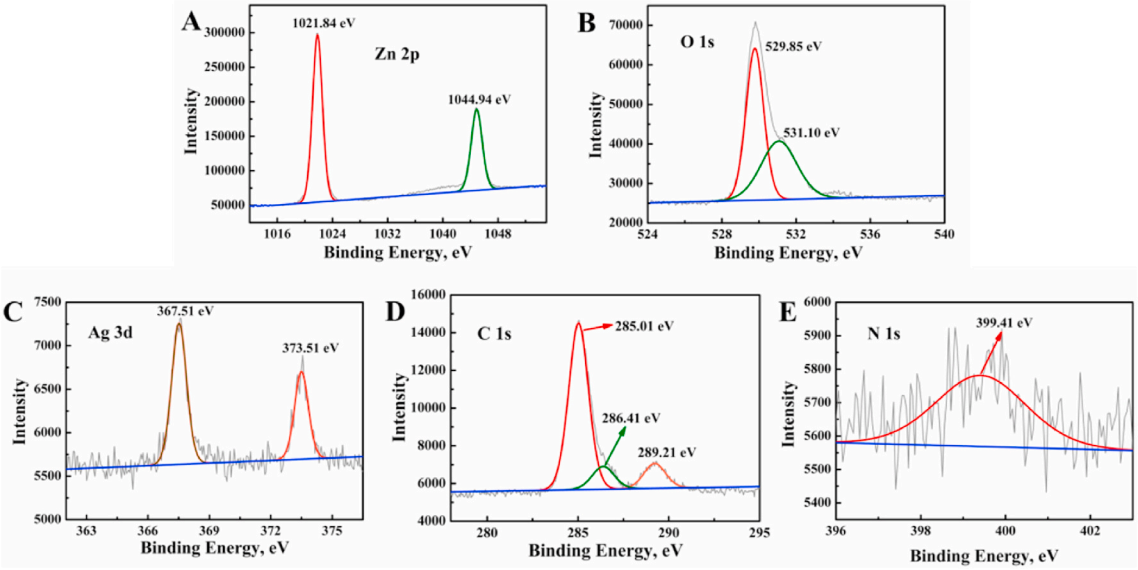

Fig. 3. XPS spectra of ZnO-AgNPs: Zn 2p (A), O 1s (B), Ag 3d (C), C 1s (D) and N 1s (E).

$$S_2O_8^{2-} + e^- \rightarrow SO_4^{2-} + SO_4^{\bullet-} \quad (3a)$$

$$ZnO\text{-}AgNPs + e^- \rightarrow ZnO\text{-}AgNPs^{\bullet-} \quad (3b)$$

$$ZnO\text{-}AgNPs^{\bullet-} + SO_4^{\bullet-} \rightarrow ZnO\text{-}AgNPs^* + SO_4^{2-} \quad (3c)$$

$$ZnO\text{-}AgNPs^* \rightarrow ZnO\text{-}AgNPs + h\nu \quad (3d)$$

In addition, the anodic ECL quenching of Ru-MOF-5 NFs by ZnO-AgNPs was tested and studied. Different modified electrodes were prepared for the ECL test under the same conditions (Fig. S6). The modified electrode of GCE/Ru-MOF-5 NFs showed intense ECL anode emission and lower ECL cathode emission. GCE/ZnO-AgNPs had only high ECL cathode emission. The GCE/Ru-MOF-5 NFs/ZnO-AgNPs modified electrode showed that the ECL anode signal was greatly reduced. The ECL stepwise characterization experimental results manifested that the anode ECL intensity of the immunosensor was obviously reduced after labeling ZnO-AgNPs on the secondary antibody (Fig. S10). The UV–vis absorption spectrum of ZnO-AgNPs has been mapped and shown absorption in the range of 377–800 nm. The measurement discovered that the ECL emission of Ru-MOF-5 NFs was at 625 nm, which is basically consistent with the fluorescence emission of 608 nm (Fig. S8).(Zhao et al., 2018) The ECL emission spectrum and ultraviolet absorption spectrum of the two were partially overlapped (Fig. S7). As a result, ECL-RET occurred and led to the quenching of Ru-MOF-5 NFs.

3.4. Characterization of the immunosensor

ECL, electrochemical impedance spectroscopy (EIS) and cyclic voltammetry (CV) were used to investigate the behavior of immunosensors during the stepwise modification. Fig. S9 and Fig. S10 showed the EIS and CV of different modified electrodes, respectively. The free transfer of electrons in bare electrode resulted in a small impedance value (Chen et al., 2017). It can be clearly noticed that the impedance value gradually increased and the current value gradually decreased with the step-by-step modification, which was put down to the free movement of electrons being hindered by nanocomposites and biomolecules. Similarly, the bare electrode has hardly any ECL emission in Fig. S11. However, two ECL signals appeared from anode and cathode when Ru-MOF-5 NFs were modified on the GCE. With the gradual modification of antibody, BSA and NSE, both anode and cathode ECL signal gradually decreased. Until Ab_2-ZnO-AgNPs were modified on the electrode, the anode and cathode ECL signals were significantly reduced and enhanced, respectively. SEM characterization for electrode fabrication was provided. As shown in Fig. S12, the morphology of the substrate is basically covered by the dripping of biomolecules including antibodies, BSA, and NSE. And then spherical nanoparticles can be observed when Ab_2-ZnO-AgNPs are modified. Accordingly, the layer-by-layer variation of EIS, ECL signal and SEM images was measured and thereby proved that the sandwich-type dual-signal immunosensor had been successfully constructed.

3.5. Optimization of the influence factors

Numerous factors that affect immunosensor performance include pH, the concentration of co-reactant, Ru-MOF-5 NFs and Ab_2-ZnO-AgNPs(Gao et al., 2017; Qian et al., 2017; Zhou et al., 2017). The sensitivity of biomolecules to the pH environment of PBS buffer led to the over acid or alkaline environment which was not conducive to the survival of biomolecules (Fig. S13). The appropriate concentration of co-reactant is essential to produce sufficient anion sulfate radical $SO_4^{\bullet-}$ (Fig. S14). Accordingly, the detection environment of PBS buffer containing 80 mmol/L of $K_2S_2O_8$ at pH 7.5 was used for the determination of the target. As shown in Fig. S15, the cathode and anode signals of the sensor changed with the concentration of Ru-MOF-5. The immunosensor had the highest ECL emission when the concentration of Ru-MOF-5 was 2 mg/mL. The influence of different concentrations of Ab_2-ZnO-AgNPs on the immunosensor was studied and the optimal concentration was 3 mg/mL (Fig. S16). In addition, the signal of the modified electrode with only different concentrations of ZnO-AgNPs was measured. As shown in Fig. S17, ZnO-AgNPs can only generate cathode signals, and the maximum ECL intensity is 3 mg/mL. It is further proved that 3 mg/mL of ZnO-AgNPs is the optimal choice to fabricate the immunosensor. Through a series of optimization experiments, 2 mg/mL of Ru-MOF-5 NFs and 3 mg/mL of ZnO-AgNPs were used to construct the immunosensor.

3.6. Performance of the immunosensor

Under the optimal conditions, the immunosensor was constructed with a series of NSE concentrations to test its performance. As shown in Fig. 4D, as the NSE concentration increases, the ECL signals of anode and cathode decrease and increase, respectively. Furthermore, three kinds of calibration curves with different ordinate meanings as shown in Fig. 4A–C. There were linear relationships between ECL intensity and NSE concentration within range of 0.0001–200 ng/mL. Obviously, the ratio of $ECL_{cathode}$ to ECL_{anode} had a better linear correlation with NSE concentration, and the immunosensor obtained a detection limit of 0.041 pg/mL. Table S1 displayed the comparison of our work with other published methods, which demonstrated that the proposed immunosensor had excellent performance in detecting NSE.

3.7. Stability, specificity and repeatability of ECL immunosensor

Various experiments were executed to examine the stability, repeatability and specificity of the immunosensor (Fig. 5). The sensors modified with different NSE concentrations remained high stability after scanning for a long time (Fig. 5A). The performance of the sensors can still maintain more than 90% after being placed for 7 days at 4 °C (Fig. 5B). The sensors were modified with different antigens, such as carcino-embryonic antigen (CEA), prostate specific antigen (PSA), insulin and the mixture (Fig. 5C). It was found that the immunosensor displayed effective specificity through testing the ECL intensity of the immunosensor. In addition, the reproducibility measurement was carried out on the identical seven modified electrodes, which showed excellent reproducibility and relative standard deviation (RSD) of 2.2% and 2.8% (Fig. 5D).

In addition, we conducted more comprehensive research on the reproducibility (Fig. S18) and 7 days stability (Fig. S19) of the immunosensor. The RSD of reproducibility was calculated at 1.3% for the selected cathode-anode ratio. And the ECL intensity remained stable at the original 99.004% after 7 days. The results showed that the reproducibility and 7 days stability of the cathode-anode ratio test were obviously better than that of the cathode or anode test.

3.8. Real sample analysis

The recovery experiment was operated to determine the content of NSE in human serum for further ascertaining the practicability of the immunosensor. Three actual samples were added with various concentrations of NSE antigen standard solution and eleven groups of parallel experiments were carried out. Table S2 showed the RSD and recovery in the range of 2.1–4.0% and 97.5–102%, respectively. The above experiments testified that the prepared sensor had satisfactory practicability for the sensitive and accurate detection of NSE.

4. Conclusion

We have constructed an immunosensor based on ZnO-AgNPs and dual-signal Ru-MOF-5 NFs as secondary antibody marker and substrate material respectively for accurate and sensitive detection of NSE. ZnO-AgNPs can efficiently quench the anode ECL emission (1.5 V) of Ru-

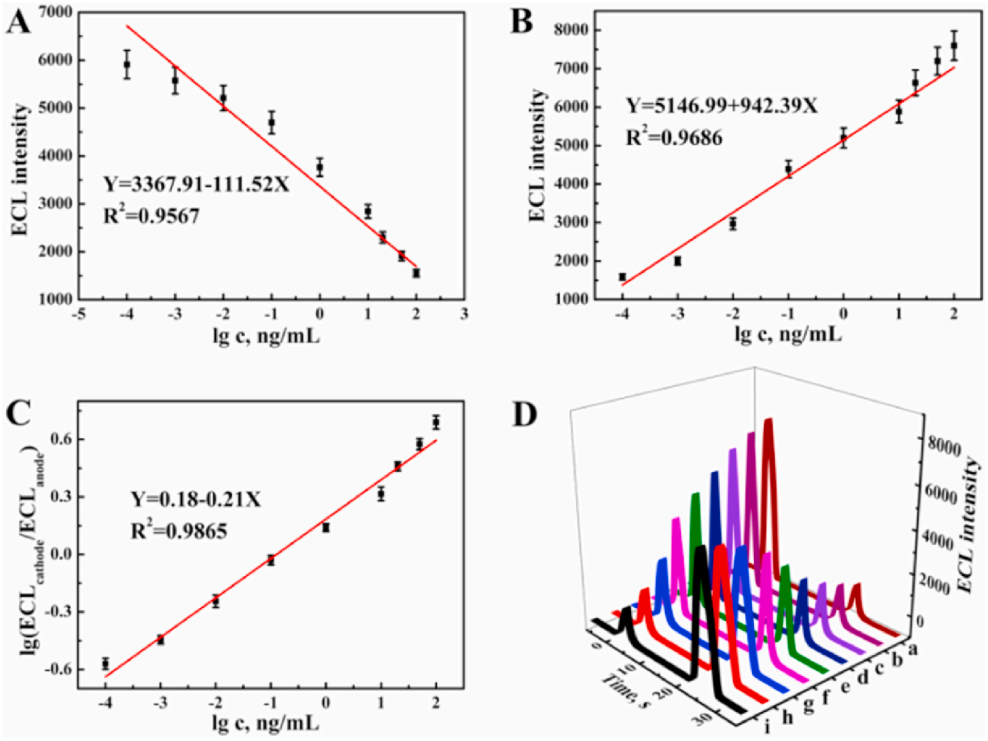

Fig. 4. The calibration plots of NSE concentration and anode ECL intensity (A), cathode ECL intensity (B), the ratio of cathode to anode ECL intensity (C); ECL intensity of immunosensors with NSE concentration within range of 0.0001–200 ng/mL (D).

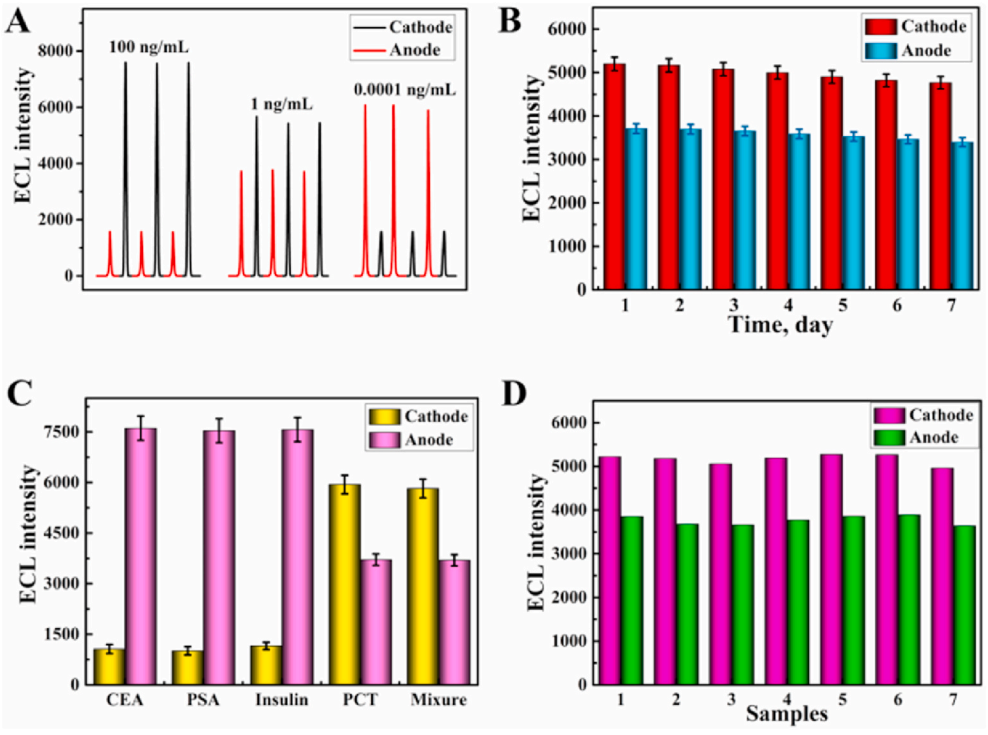

Fig. 5. The multiple scan stability (A) of immunosensor; 7 days stability (B), specificity (C) and reproducibility (D) of immunosensor incubated with 1 ng/mL NSE.

MOF-5 NFs and enhance the cathode ECL signal (−1.5 V) of the immunosensor. The "dual-potential" ratiometric ECL immunosensor is able to efficiently reduce the probability of false positive in biomolecule detection as well as build up the exactitude of assessment. The performance characterization and actual sample analysis show that the sensor has remarkable performance and high potential in future clinical detection.

CRediT authorship contribution statement

Xue Dong: Conceptualization, Data curation, Writing – original draft. **Yu Du:** Writing – review & editing. **Guanhui Zhao:** Methodology, Data curation. **Wei Cao:** Methodology, Writing – review & editing. **Dawei Fan:** Data curation. **Xuan Kuang:** Formal analysis. **Qin Wei:** Funding acquisition, Project administration. **Huangxian Ju:** Formal analysis.

Declaration of competing interest

The authors declare that they have no known competing financial interests or personal relationships that could have appeared to influence the work reported in this paper.

Acknowledgments

This study was supported by the Innovation Team Project of Colleges and Universities in Jinan (No. 2019GXRC027), the Special Foundation for Taishan Scholar Professorship of Shandong Province, the National Key Scientific Instrument and Equipment Development Project of China (No. 21627809), the National Natural Science Foundation of China (No. 21777056), and the Jinan Scientific Research Leader Workshop Project (2018GXRC021 and 2018GXRC024).

Appendix A. Supplementary data

Supplementary data to this article can be found online at https://doi.org/10.1016/j.bios.2021.113505.

References

Adsetts, J.R., Hoesterey, S., Gao, C., Love, D.A., Ding, Z., 2020. Langmuir 36, 14432–14442.
Bandyopadhyay, S., Hennes, H., Gorelick, M.H., Wells, R.G., Walsh-Kelly, C.M., 2014. Acad. Emerg. Med. 12, 732–738.
Chen, A., Zhao, M., Zhuo, Y., Chai, Y., Yuan, R., 2017. Anal. Chem. 89, 9232–9238.
Farzad, Z., Ali, G., Mohammad Boshra, M.-E., Mona, T., 2020. Green Chem. 22, 7265–7300.
Feng, L., Wu, L., Hu, L., Ren, J., Xing, F., 2017a. Biosens. Bioelectron. 98, 378–385.
Feng, Q.M., Shen, Y.Z., Li, M.X., Zhang, Z.L., Chen, H.Y., 2017b. Anal. Chem. 88, 937.
Forgan, R.S., Smaldone, R.A., Gassensmith, J.J., Furukawa, H., Cordes, D.B., Li, Q., 2012. J. Am. Chem. Soc. 134, 406–417.
Fu, X., Tan, X., Yuan, R., Chen, S., 2017. Biosens. Bioelectron. 90, 61–68.
Gao, F., Zhou, F., Chen, S., Yao, Y., Wu, J., Yin, D., Geng, D., Wang, P., 2017. Analyst 142, 4308–4316.
Gao, H., Zhang, J., Liu, Y., Tu, W., Dai, Z., 2019. Anal. Chem. 91, 12038–12045.
Ghosh, S., Goudar, V.S., Padmalekha, K.G., Bhat, S.V., Indi, S.S., Vasan, H.N., 2012. RSC Adv. 2, 930–940.
Guo, J., Li, S., Wang, S., Wang, J., 2020. J. Agric. Food Chem. 68, 12738–12748.
Huang, X., Chen, Y., Feng, X., Hu, X., Liu, L., 2020. J. Membr. Sci. 602, 117956.
Isgrò, M., Bottoni, P., Scatena, R., 2015. Adv. Exp. Med. Biol. 867, 125–143.
Leff, E.L., Brooks, J., Trojanowski, J.Q., 2015. Cancer 56, 625–631.
Li, L., Chen, Y., Zhu, J., 2017. Anal. Chem. 89, 358–371.
Li, M., Jiao, L., Liu, S., Zhang, L., Li, H., 2019. Anal. Chim. Acta 1086, 103–109.
Li, W., Liu, P., Liu, Z., Cao, H., Ye, S., Zhao, k., Liang, G., Zhu, J., 2020. Sensor. Actuator. B Chem. 327, 128890.
Liu, Z., Qi, W., Xu, G., 2015. Chem. Soc. Rev. 44, 3117–3142.
Lv, W., Ye, H., Yuan, Z., Liu, X., Yang, W., 2019. Trac. Trends Anal. Chem. 123, 115767.
Qian, Y., Fan, T., Wang, P., Zhang, X., Luo, J., Zhou, F., Yao, Y., Liao, X., Li, Y., Gao, F., 2017. Sensor. Actuator. B Chem. 248, 187–194.
Raja, A., Rajasekaran, P., Vishnu, B., Selvakumar, K., Do, J., Swaminathan, M., Kang, M., 2020. Separ. Purif. Technol. 252, 117446.
SavićBiserčić, M., Marjanović, B., NedićVasiljević, B., Mentus, S., Zasońska, B.A., Ćirić-Marjanović, G., 2019. Microporous Mesoporous Mater. 278, 23–29.
Shang, L., Wang, X., Zhang, W., Jia, L., Ma, R., Jia, W., Wang, H., 2020. Sensor. Actuator. B Chem. 325, 128776.
Shi, L., Li, X., Zhu, W., Wang, Y., Pang, X., 2017. ACS Sens. 2, 1774–1778.
Wang, L., Yue, Q.L., Li, H.B., Xu, S.L., Liu, P., 2012. Sci. China Chem. 56, 86–92.
Wang, L., Zhu, Y., Du, C., Ma, X., Cao, C., 2020. J. Mater. Chem. A. 8, 24895–24919.
Ye, J., Zhu, L., Yan, M., Zhu, Q., Yang, X., 2018. Anal. Chem. 91, 1524–1531.
Zhang, Q., Chou, T.P., Russo, B., Jenekhe, S.A., Cao, G., 2010. Adv. Funct. Mater. 18, 1654–1660.
Zhao, G., Wang, Y., Li, X., Dong, X., Wang, H., Du, B., Cao, W., Wei, Q., 2018. ACS Appl. Mater. Interfaces 10, 22932–22938.
Zhao, G., Wang, Y., Li, X., Yue, Q., Dong, X., Du, B., Cao, W., Wei, Q., 2019. Anal. Chem. 91, 1989–1996.
Zhao, H., Song, H., Chou, L., 2014. Mater. Chem. Phys. 143, 1005–1011.
Zhou, F., Yao, Y., Luo, J., Zhang, X., Zhang, Y., Yin, D., Gao, F., Wang, P., 2017. Anal. Chim. Acta 969, 8–17.
Zhou, H., Ding, K., Yu, Q., Wang, H., Liu, J., Wang, Z., 2021. Biosens. Bioelectron. 189, 113367.